



Drag, lift, and buoyancy forces on a single large particle in dense granular flows

Arjun V. Yennemadi  and Devang V. Khakhar **Department of Chemical Engineering, Indian Institute of Technology Bombay, Powai, Mumbai 400076, India*

(Received 17 March 2023; accepted 2 June 2023; published 13 July 2023)

We study size segregation in the limit of a single large particle (intruder) embedded within a flowing granular layer. Using discrete-element-method-based computations, we calculate and characterize the drag, lift, and buoyancy forces experienced by the intruder in two systems: (1) a simple shear flow without gravity and (2) gravity-driven flow down an inclined plane. In agreement with previous studies, the drag force in both systems is seen to follow Stokes' Law with a slightly different constant. However, in contrast with previous work, we report that lift force does not follow the Saffman relation; instead, its variation is captured effectively using a size-corrected Stokes' Law. The buoyancy forces calculated in our work scale in a manner that compares well with previous studies. The computed effective volumes of the intruders were found to be close to previously reported values, and the buoyancy force calculated using this effective volume was found to be significantly lower than our computed buoyancy force, suggesting contributions from other factors. Analysis of the relative velocity and stress in the neighborhood of the intruder shows that the lift force is caused by a net upward collisional stress arising from a higher relative inward velocity in the lower part of the intruder due to a positive slip velocity. The buoyancy force is higher than that predicted by Archimedean buoyancy due to large fluctuations in the pressure near the intruder. A continuum model for the segregation flux is presented based on the computed drag, lift, and buoyancy forces.

DOI: [10.1103/PhysRevFluids.8.074301](https://doi.org/10.1103/PhysRevFluids.8.074301)

I. INTRODUCTION

Spontaneous separation of particles in flowing granular mixtures, or segregation, is a commonly observed phenomenon in natural processes and has important practical implications [1–4]. Segregation is driven by differences in properties of the mixture constituents, for example, size, density, shape, or roughness. The early works of Drahn and Bridgwater [5], Savage and Lun [6], and Jenkins and Mancini [7], using different approaches, provided the first mechanistic understanding of the process. Since then, granular segregation has been the subject of considerable research, summarized in reviews by Ottino and Khakhar [1] and Gray [4]. More recently, particle-level computational approaches such as the discrete element method (DEM) have allowed a deeper investigation of the mechanisms underlying segregation [8–16], and this approach is used in the present work. A review of prior work using this method is given below.

DEM is well suited to calculate the forces acting on the different species in the granular mixture, which are the basis of segregation. Consider first the case of density segregation in a flowing mixture, that is, the segregation of particles of different densities but equal size, in which heavier particles sink and lighter particles rise. Tripathi and Khakhar [8] studied the terminal sedimentation velocity of a single particle (or *intruder*) of different density (ρ_i) but the same size (d) as particles

*khakhar@iitb.ac.in

flowing down an inclined plane. Considering the flowing particles to be a fluid of density $\rho\phi$, they found that the intruder experiences a drag force given by Stokes' Law: $F_D = C_D\eta du_s$, where ρ is the particle density, ϕ is the volume fraction of solids, u_s is the particle velocity, η is the apparent viscosity of the flowing particles, and C_D is a constant of value between 3.1π and 3.7π , slightly greater than what is observed in the case of fluids. The buoyancy force was found to be equal to the Archimedean buoyancy, but with the effective volume of the test particle given by V_i/ϕ , where V_i is the volume of the intruder. The effective volume is calculated from the requirement that the buoyancy force must be equal to the weight of the intruder when its density is equal to that of the flowing particles ($\rho_i = \rho$). Tripathi and Khakhar [9] then extended these results to mixtures of heavy and light particles and obtained good agreement between the predictions of the theory and DEM simulation results for mixtures.

The size segregation in flowing mixtures of particles with equal density but a different size is more complex. In this case, the larger particles rise and the smaller particles sink, which is not predicted by kinetic theory [17]. In the absence of other forces, this requires the buoyancy force to be larger than the weight of the particle. Guillard *et al.* [10] carried out a two-dimensional DEM study of the segregation force of a large intruder disk in a shear flow of smaller disks between parallel plates with gravity. A spring force is applied on the intruder normal to the flow direction. The segregation force is computed from the mean extension of the spring. The segregation force was correlated with the pressure gradient, the shear stress gradient, and the effective friction (μ), which is the ratio of the shear stress to the pressure. All the data collapsed to a single curve using two empirical functions of μ .

The forces on an intruder were studied in detail by van der Vaart *et al.* [11] by considering a single large particle in an inclined plane system, similar to [8]. The effective volume of the large particle is obtained using Voronoi tessellation, and Kumar *et al.* [13] showed that these values were close to the partial molar volume of the large particle computed from kinetic theory. The net upward force on the particle due to the flowing bed was found by imposing a linear spring force on the particle, as in the work by Guillard *et al.* [10]. The lift force on the particle was then calculated by subtracting the Archimedean buoyancy force, computed using the effective volume, from the upward force due to the bed. In their work, van der Vaart *et al.* [11] measured the particle's slip velocity and related it to the lift force using the theory of Saffman Lift [18]. However, the slip velocities are very close to zero with significant error bars since the net body force on the intruder in the direction of flow was very small. More recently, van Schroyensteen Lantman *et al.* [15] have computed the pressure in the neighborhood of an intruder and showed that Archimedean buoyancy is lower than the upward force experienced by the intruder, in agreement with the results of van der Vaart *et al.* [11].

Adopting the same spring force approach, Jing *et al.* [14] carried out an extensive study using DEM of the segregation of a single large particle in an inclined plane flow and a shear flow with gravity. They found that the total upward force due to the bed, scaled using the Archimedean buoyancy force based on the particle volume (rather than the effective volume), was a function of the size ratio (S) alone for a wide range of system parameters. An empirical fit to the data was presented and it was seen that the scaled segregation force was larger than the component of the weight of the intruder for $1 < S < 4$, indicating that intruders within this size range would rise, whereas those outside it would sink. In subsequent work, Jing *et al.* [16] obtained a scaling law for the segregation force by decomposing it into two terms: First, a gravity-induced pressure gradient term similar to buoyancy, and a second shear rate gradient term, both shown to be a function of the particle size ratio alone. Duan *et al.* [19] extended this approach to bidisperse flowing granular mixtures with arbitrary concentrations of small and large particles and predicted the concentration below which results for single intruders would remain applicable.

In the present work, we compute the lift, drag, and buoyancy forces acting on a single large particle (intruder) in a dense granular flow using DEM simulations. The intruder is constrained by a linear spring in the direction normal to the flow as in [10]. A pulling body force F_p (positive or negative) is imposed on the intruder in the direction of the flow to generate significant slip velocities to enhance the accuracy of our subsequent force calculations. Two systems are studied: (1) a simple

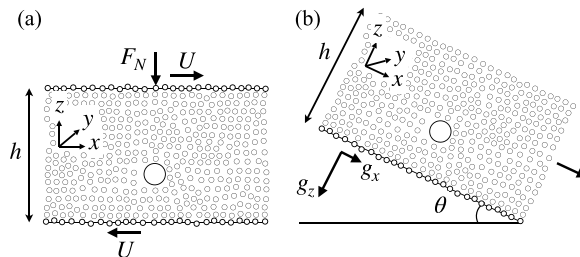


FIG. 1. Schematic view of the systems used in the simulations. (a) Shear flow of layer thickness h , with wall velocity of U and a force F_N acting on each particle of the upper wall. (b) Inclined plane flow of layer thickness h , at an inclination angle θ . The components of the gravitational acceleration vector are indicated.

shear flow without gravity to compute the lift and drag forces in the absence of buoyancy, and (2) flow down an inclined plane. In the latter case, the drag, lift, and buoyancy forces on the intruder are individually calculated by carrying out simulations for different values of the pulling force (F_P). The work aims to develop both a qualitative and quantitative understanding of the effect of intruder size and local shear rate on the lift, drag, and buoyancy forces on an intruder, while improving upon previous work in terms of the accuracy of computations. The relative velocity and stress in the neighborhood of the intruder are also studied to gain insight into the causes of the forces experienced by the intruder. Computational details are given next, followed by the results of the study, which includes a brief discussion of the application of the results to segregation in sheared binary mixtures. The conclusions are given in the final section.

II. COMPUTATIONAL DETAILS

Systems. The flow of particles with a nominal diameter d and an intruder of diameter d_i is simulated using the discrete element method in two systems: (1) a gravity-free shear flow and (2) a gravity-driven flow on a rough inclined plane, shown schematically in Fig. 1. The shear flow is generated by parallel plates composed of particles of diameter d arranged on a square lattice, moving in opposite directions with a velocity U . The plates are made rough by displacing their particles through a random distance in the range $(0, d)$ along the inward surface normal. The inclined plane has the same configuration, except that the random displacement is instead in the range $(0, 1.5d)$. The shear flow is generated at constant pressure by allowing the upper plate to move in the z direction and applying a constant force F_N in the $-z$ direction on each particle of the plate. The simulation box has a cross section $25d \times 25d$ in the xy plane and a height of about $40d$. Periodic boundary conditions are applied in the x and y directions. The lift force is sensitive to the cross-sectional dimensions and we use sufficiently large values so that further increase does not affect the results. Here, 25 000 particles form the bulk medium and a polydispersity in size is used with diameters uniformly distributed in the range $(0.9d, 1.1d)$ to prevent crystallization. A single intruder, characterized by a size ratio $S = d_i/d$, is used in each simulation. The density ρ of the particles and the intruder are the same. In both systems, the position of the intruder is constrained in the z direction by the application of a spring force,

$$F_S = K(z_i - z_0), \quad (1)$$

where z_i is the position of the intruder, z_0 is the zero force position, and K is the spring stiffness. In addition, we apply a pulling force on the intruder, F_P , in the x direction. In the case of the inclined plane flow, the pulling force results in a higher mean velocity. To counteract this, a reaction force $-F_P/25\,000$ is applied on each bulk particle.

Parameters. The simulations are carried out using the LAMMPS package [20]. We take $d = 0.1$ cm and $\rho = 2.5$ g/cm³ in all the simulations. Intruders of sizes corresponding to the size ratios $S = 1$,

TABLE I. Parameter values used in the DEM simulations.

Parameter	Dimensionless value	Value in cgs units
k_t	2×10^7	2568000
k_t/k_n	2/7	2/7
γ_n	50.0	4952.0
γ_t	0.0	0.0
e_n	0.88	0.88
e_t	1	1
μ	0.5	0.5

2, 3, 4, 5, and 6 are used. The Hookean spring model with viscous dissipation and friction corresponding to the L3 model of Silbert *et al.* [21] is used to calculate the interparticle forces, and the parameter values are listed in Table I. In the shear flow, we take the normal force to be $F_N = 3$ dyn per particle, which results in a pressure of 300 dyn/cm², and different wall velocities, $U = 25, 50, \text{ and } 100$ cm/s. Three angles are used for the inclined plane simulations, $\theta = 25, 26, \text{ and } 27^\circ$.

The spring force parameters used are $K = 20$ dyn/cm and $z_0 = 20d$ in both systems; however, for large intruders ($S > 4$) in the inclined plane system, we use $K = 40$ dyn/cm and $z_0 = 25d$. Such values are chosen to ensure that the intruder is roughly in the middle of the flowing layer, and the results are independent of the values of K and z_0 . Simulations with different pulling force values, positive and negative, are carried out to generate a range of slip velocities. For the shear flow, we use $F_p = -5S, -2.5S, 2.5S, \text{ and } 5S$, and for the inclined plane flow, we use $F_p = -10S, -5S, 5S, \text{ and } 10S$. Different values of F_p are used so as to obtain similar slip velocities, accounting for the higher resistance of larger particles and the higher viscosity of the inclined plane flow. The integration time step used was $dt = 10^{-6}$ s, which is 1/50th of the time of a collision. To attain a steady state, we first simulated the flows with $dt = 10^{-5}$ s for 10 s and then for 1 s with a time step $dt = 10^{-6}$ s. Steady-state data are generated over a run of 10 s with $dt = 10^{-6}$ s, corresponding to 10^7 steps, and split into 20 sets of duration 0.5 s each. The protocol is repeated three times for each parameter set, starting with different random seeds, yielding 60 data sets, which are used to calculate the mean value and standard error for quantities of interest, discussed below. Additional simulations are carried out for both systems with $S = 4$ to study the flow and stress in the neighborhood of the intruder.

In addition, simulations to determine the effective volume of an intruder (V_E) are carried out for an inclined plane system of size $12d \times 12d \times 40d$, with an angle of inclination 25° and 8000 base particles. Here, n_i well-separated intruder particles are added and we compute the resulting increase in the height of the flowing layer (Δh). The number of intruders (n_i) is such that the total volume of the intruders is about $64V$, where $V = \pi d^3/6$ is the volume of a base particle. This gives an increase in the height of about 0.15%.

Analysis. The primary data generated from the simulations are the mean position of the intruder, \bar{z}_i , which yields the mean value of the spring force, \bar{F}_S from Eq. (1), and the mean slip velocity, defined as

$$u_s = u_i - u(\bar{z}_i), \quad (2)$$

where u_i is the mean velocity of the intruder in the x direction and $u(\bar{z}_i)$ is the mean velocity of the bulk particles at the mean position of the intruder. The mean slip velocity is calculated by approximating the mean velocity of the bulk particles to be locally linear.

In the case of the shear flow system at steady state, the lift force is equal to the spring force,

$$F_L = F_S(\bar{z}_i), \quad (3)$$

and the mean drag force is equal to the pulling force applied on the intruder,

$$F_D = F_P. \quad (4)$$

We correlate the drag force using a Stokes' Law-type scaling of the form

$$F_D = C_D \eta d_i u_s, \quad (5)$$

where C_D is a constant, $\eta = \tau_{xz}/\dot{\gamma}$ is the apparent viscosity, τ_{xz} is the shear stress, and $\dot{\gamma} = (du/dz)|_{\bar{z}_i}$ is the shear rate at the mean position of the intruder. The latter two are computed for simulations of the system without the intruder.

For the inclined plane system at steady state, the spring force is given by

$$F_S(\bar{z}_i) = F_L + F_{Bz} - F_{gz}, \quad (6)$$

where F_{Bz} is the component of the buoyancy force in the z direction, $F_{gz} = m_i g \cos \theta$ is the component of the weight of the intruder in the $-z$ direction, and m_i is the mass of the intruder. To obtain the buoyancy force and the lift force from the computed spring force, we assume that the buoyancy force is independent of the slip velocity (u_s), and the lift force is dependent on the slip velocity [$F_L = F_L(u_s)$]. The buoyancy force is then calculated from the spring force at $u_s = 0$, i.e., when there is no lift force ($F_L = 0$). Similarly, the pulling force at steady state is

$$F_P = F_D + F_{Bx} - F_{gx}, \quad (7)$$

where F_{Bx} and F_{gx} are components of the buoyancy force and weight in the x direction. Again the buoyancy force is calculated from Eq. (7) at $u_s = 0$, which corresponds to a zero drag force ($F_D = 0$). The solid fraction (ϕ), velocity (v_x), and shear stress (τ_{xz}) profiles are computed over the height of the systems (z), using bins of height d to characterize the flows.

The effective volume of the intruder (V_E) is calculated from the change in the free surface height (Δh) as

$$V_E \equiv \Delta V_{\text{bed}} = \Delta h L_x L_y / n_i, \quad (8)$$

assuming that the increase in system volume on the addition of intruders, for all other conditions remaining constant, is the effective volume occupied by the intruders. As shown in Sec. III C, V_E is larger than V_i , the intruder volume, and corresponds to the volume of the intruder along with a portion of the void space around it. As computed, V_E is the partial molar volume of the intruder at infinite dilution.

The local two-dimensional velocity distribution and stress distribution are computed in a neighborhood of the intruder in a vertical slice of thickness d passing through the center of the intruder and in a layer adjacent to the intruder surface. In addition to the two-dimensional distributions, two types of profiles are presented: Variation with the height relative to the intruder and variation over the circumference in a vertical plane passing through the center of the intruder.

III. RESULTS AND DISCUSSION

In the following sections, we first present results for the shear flow system followed by the inclined plane flow system. Analysis of the lift, drag, and buoyancy forces in the two systems is presented next. Results for the variation of solid fraction, velocities, and stresses in the neighborhood of the intruder are given in the final section.

A. Shear flow system

The computed steady-state profiles for the system are shown in Fig. 2 for an intruder with a size ratio $S = 6$ (solid lines). A linear velocity profile and a constant shear stress of about 150 dyn/cm² are obtained for the shear flow. The solid fraction is nearly constant with height. Distortions in the three profiles are clearly seen in the interval $z \in (2, 2.5)$ cm, which corresponds to the location of

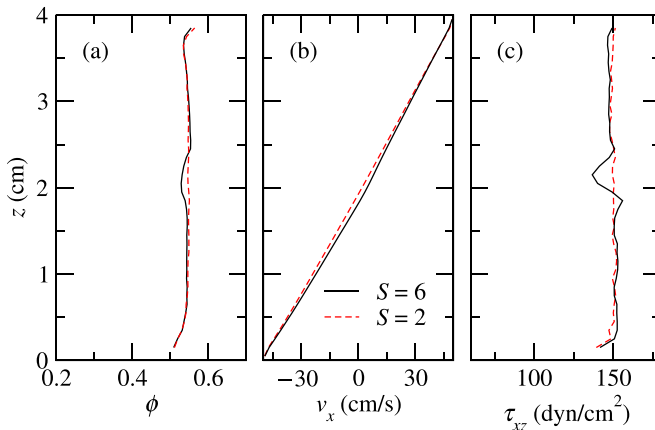


FIG. 2. Variation of the (a) solid fraction ϕ , (b) velocity v_x , and (c) shear stress τ_{xz} for the shear flow for $U = 50$ cm/s and two different intruder sizes.

the intruder. For other, smaller intruders, the degree of distortion is considerably smaller, as can be seen for the profiles for $S = 2$, also shown in Fig. 2 (dashed lines). The results are representative of the general trends in the velocity, shear stress, and volume fraction over all combinations of S and U studied.

Figure 3 shows the variation of the spring force (F_S) and the slip velocity (u_s) with the pulling force (F_P) for three different intruder sizes (S). The variation of both F_S and u_s is linear with F_P . In this case, the spring force is equal to the lift force (F_L), and the pulling force is equal to the drag force (F_D). The results indicate that the lift force is proportional to the drag force ($F_L \propto F_D$), and the drag force is proportional to the slip velocity ($F_D \propto u_s$). Further, the lift force and the slip velocity are zero for $F_P = 0$, as might be expected from the system's symmetry, and the direction of the lift force is in the positive z direction. For a fixed pulling force, the lift force (F_L) and slip velocity (u_s) decrease with an increase in intruder size (S). The dashed lines in the figure are the linear least-squares fit to the data of the form $F_L = R F_D$ and $u_s = F_D / \xi$, where R and ξ are the fitting constants. Similar results are obtained for the other intruder sizes (S) and plate velocities (U) considered.

B. Inclined plane flow

The computed profiles for the inclined flow system are shown in Fig. 4 for an intruder with a size ratio $S = 6$. The velocity profile is a Bagnold profile [21] and the stress increases linearly with depth. The solid fraction is nearly constant with height in the system, as for the shear flow (Fig. 2).

We define the forces $F_{Tx} = F_P + F_{gx}$ and $F_{Tz} = F_S + F_{gz}$, which correspond to the total bed force on the intruder in the $-x$ and z directions, respectively. Figure 5 shows the variation of these forces (F_{Tx}, F_{Tz}) versus the slip velocity (u_s). The forces F_{Tx} and F_{Tz} both vary linearly with the slip velocity (u_s) over the range of pulling forces used, and both increase with intruder size for a fixed slip velocity (u_s). The data are plotted in this form to facilitate analysis using Eqs. (6) and (7), which can be written as

$$F_{Tx} = \xi u_s + F_{Bx}, \quad (9)$$

$$F_{Tz} = R \xi u_s + F_{Bz}, \quad (10)$$

taking the drag force to be $F_D = \xi u_s$ and the lift force to be $F_L = R \xi u_s$. The dashed lines in the figure are linear least-squares fits of the above equations to the data taking ξ , R , F_{Bx} , and F_{Bz} as

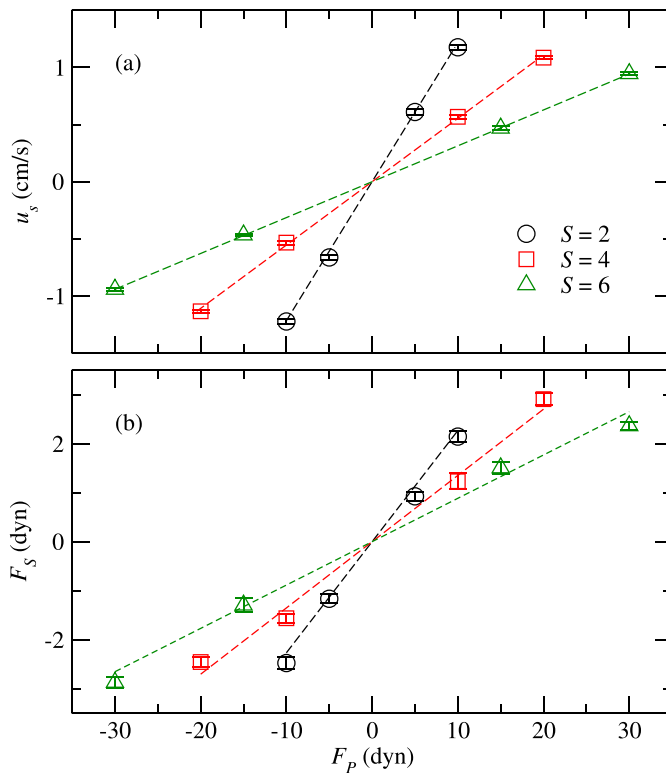


FIG. 3. Variation of (a) the spring force (F_s) and (b) the slip velocity (u_s) with the pulling force (F_p) in the shear flow system for three different intruder sizes (S), for a wall velocity, $U = 50$ cm/s. The error bars indicate the standard error and the dashed lines are linear least-squares fits to the data.

fitting constants. The fits, thus, yield the drag, lift, and buoyancy forces for each intruder size (S) and inclined plane angle (θ). Similar results are obtained for the other intruder sizes and inclined plane angles studied here. Figure 6 shows the variation of the lift force (F_L) with the drag force (F_D), which is linear. As found for the shear flow, the lift force acts upward for a positive slip velocity.

C. Scaling relations

We consider here the scaling behavior of the drag, lift, and buoyancy forces computed for the two systems. Anticipating a Stokes' Law scaling for the drag force [Eq. (5)], Fig. 7 shows a plot of the drag force (F_D) versus $\eta d_i u_s$ for all the data for both systems, as indicated in the legend. The data collapse to a single line and the dashed line is a linear least-squares fit of Eq. (5) to the data taking C_D to be a fitting parameter. The fitted coefficient C_D is slightly lower than that obtained by Tripathi and Khakhar [8], which may be due to the larger system used in the present work. The Stokes' Law scaling is reasonable on dimensional grounds since the particle Reynolds number $\text{Re} = \rho \phi d_i^2 \dot{\gamma} / \eta$ is less than 2 in all cases, implying that inertial effects are negligible. Here, the shear rate is given by $\dot{\gamma} = |du/dz|$.

We first consider scaling of the lift force using the theory of Saffman [18] and Stone [22], which gives the lift force as

$$F_L = -1.615(\rho \phi \eta \dot{\gamma})^{1/2} d_i^2 u_s, \quad (11)$$

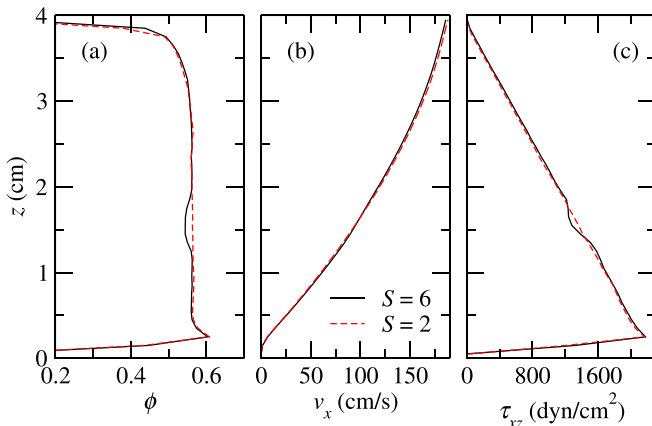


FIG. 4. Variation of the (a) solid fraction ϕ , (b) velocity v_x , and (c) shear stress τ_{xz} for the inclined plane flow for an inclination angle $\theta = 25^\circ$ and two intruder sizes.

for $du/dz > 0$. The theory predicts that the lift force acts in the $-z$ direction for a positive slip velocity u_s , which is opposite to the results obtained here. We thus consider only the magnitude of

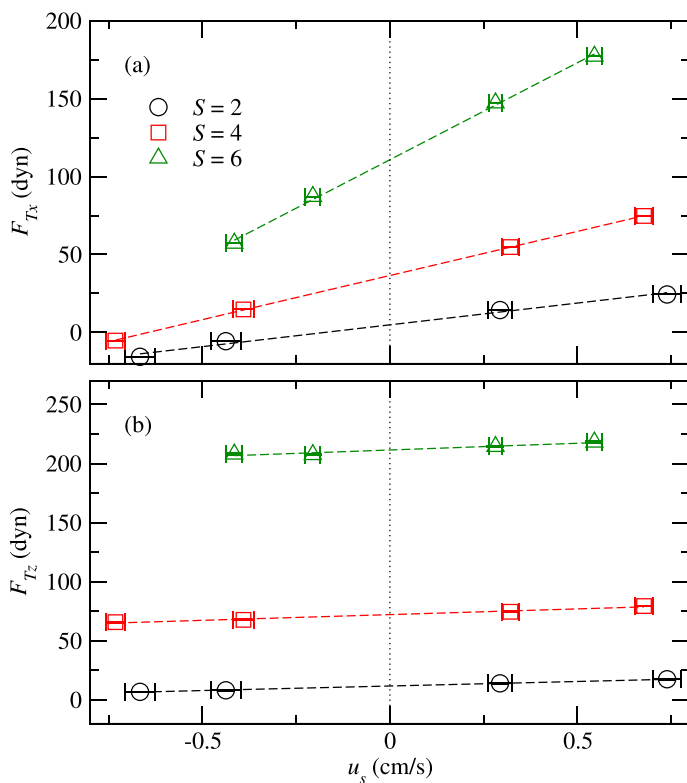


FIG. 5. Variation of the components of the total applied force on the intruder with slip velocity (u_s): (a) x component (F_{Tx}) and (b) z component (F_{Tz}). The error bars indicate the standard error and the dashed lines are linear least-squares fits of Eqs. (9) and (10) to the data.

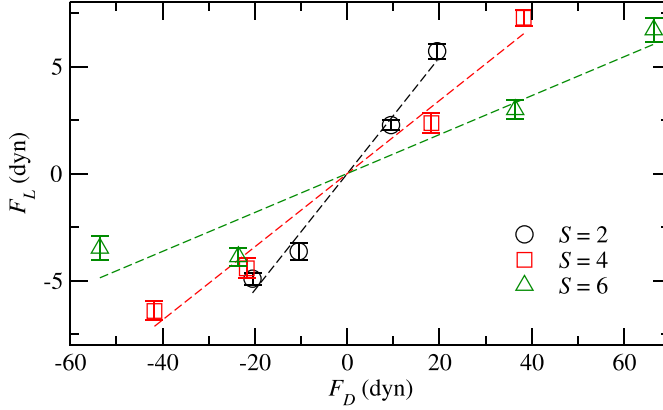


FIG. 6. Variation of the lift force (F_L) with drag force (F_D) for three intruder sizes (S). The error bars indicate the standard error and the dashed lines are linear least-squares fits to the data.

the force in the scaling. From Eq. (11), the ratio $R = F_L/F_D$ is given by

$$R = C_L \sqrt{\text{Re}}, \quad (12)$$

where C_L is a constant. Figure 8 shows a plot of R versus $\sqrt{\text{Re}}$ for all the data. The results indicate that the data do not conform to the Saffman theory, even in magnitude.

Based on the finding that $F_L \propto F_D$ and that the lift force decreases with increasing intruder size, we consider next an empirical scaling of the form $R = A - BS$ or, equivalently,

$$F_L = F_D(A - BS) = 2.52\pi\eta d_i u_s (A - BS), \quad (13)$$

where A and B are constants. Fitting Eq. (13) to all the data gives $A = 0.27 \pm 0.02$ and $B = 0.028 \pm 0.005$, and a comparison of the predictions of Eq. (13) to the simulation data is shown in Fig. 9. The match between the two is reasonably good. The results indicate that the lift force is 10–30% of the drag force, with the ratio R varying linearly with the intruder size ratio S .

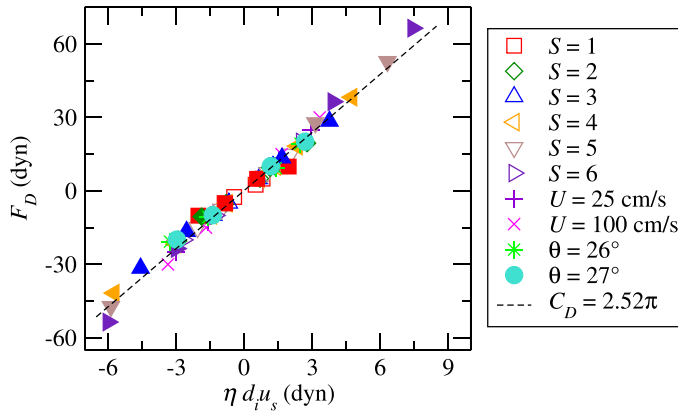


FIG. 7. Variation of the drag force (F_D) with $\eta d_i u_s$ for all the data. Empty polygonal symbols correspond to data for shear flow at wall velocity $U = 25$ cm/s and filled polygonal symbols to data for the inclined plane flow for inclination angle $\theta = 25^\circ$, for different size ratios (S) as indicated in the legend. The other symbols correspond to $S = 2$, different wall velocities (U) for shear flow, and different inclination angles (θ) for inclined plane flow. The dashed line is a linear least-squares fit to the data.

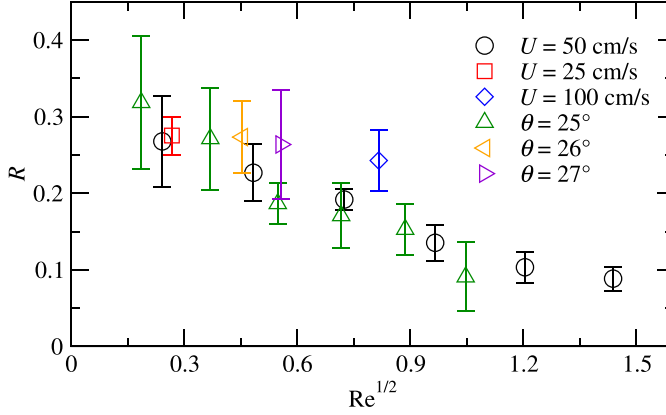


FIG. 8. Variation of the ratio of the lift force to the drag force ($R = F_L/F_D$) with $Re^{1/2}$ for all the data.

Next we consider the scaling relations for the buoyancy forces obtained from the data for the inclined plane flow. Figure 10 shows the variation of the buoyancy forces in the x and z directions scaled by the component of the weight of the particle in the corresponding direction (F_{Bx}/F_{gx} , F_{Bz}/F_{gz}) versus the intruder size ratio (S). The data for the buoyancy force in both directions collapse to a single curve. The scaled buoyancy forces are larger than unity ($F_{Bz} > F_{gz}$) for $S > 1$ and $S < 4$, indicating a net upward force on the intruder, even in the absence of a lift force. The correlation of Jing *et al.* [14] for the scaled total upward force (F_{Tz}/F_{gz}), which is a sum of the buoyancy force and the lift force, is

$$f(S) = \phi[1 - c_1 \exp(-S/R_1)][1 + c_2 \exp(-S/R_2)], \quad (14)$$

with $c_1 = 1.43$, $c_2 = 3.55$, $R_1 = 0.92$, $R_2 = 2.94$, and is shown in the figure as a dotted line. We apply a correction to the correlation by subtracting the lift force estimated from Eq. (13). In the absence of a pulling force, which corresponds to the system of Jing *et al.* [14], the drag force is given by $F_D = F_{gx} - F_{Bx}$. Using Eq. (13) and the relation $F_{Bx}/F_{gx} = F_{Bz}/F_{gz}$, the lift force is given by

$$F_L = -\alpha(F_{Bz} - F_{gz}), \quad (15)$$

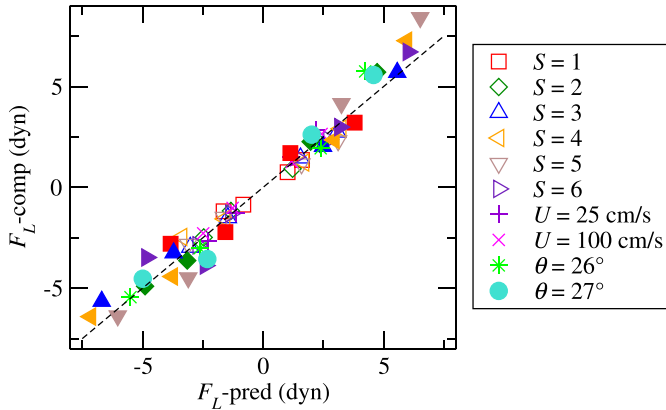


FIG. 9. Comparison of the computed lift force (F_L -comp) with the lift force predicted from Eq. (13) (F_L -pred). The symbols are the same as in Fig. 7.

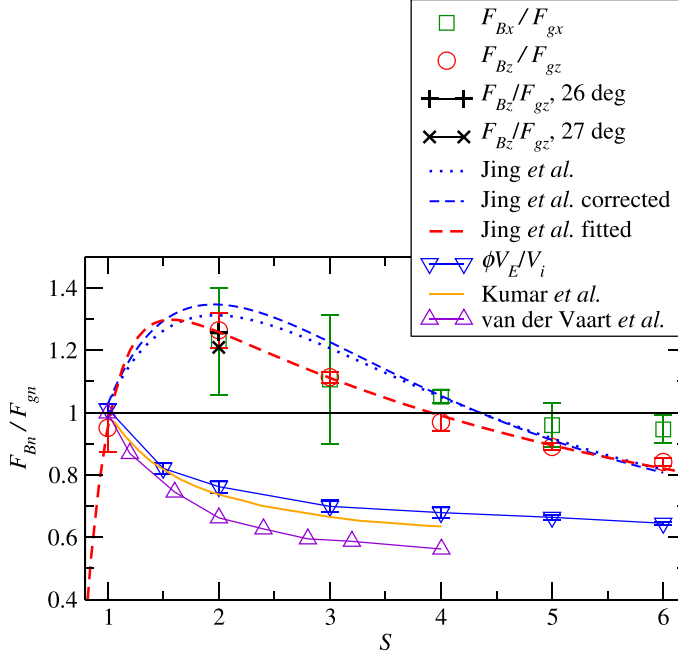


FIG. 10. Variation of the buoyancy forces in the two directions (F_{Bn} , $n = x, z$) scaled with the corresponding component of the particle weight (F_{gn} , $n = x, z$) with size ratio S for the inclined plane flow for inclination angle $\theta = 25^\circ$. Data for inclination angles $\theta = 26^\circ$ and 27° and $S = 2$ are included. The correlation of Jing *et al.* [14] [Eq. (14)] and the correlation corrected for the lift force (Jing *et al.* corrected) are shown. The correlation [Eq. (14)] fitted to the data is shown (Jing *et al.* fitted). The scaled Archimedean buoyancy forces ($\phi V_E / V_i$) using the computed intruder effective volume (V_E) are shown along with the scaled Archimedean force reported by Kumar *et al.* [13] and van der Vaart *et al.* [11].

where $\alpha = (A - BS) \tan \theta$. In this case, when $F_{Bz} > F_{gz}$, the slip velocity is negative and the lift force acts downward (in the $-z$ direction), which is opposite to the direction of the buoyancy force. Finally, from $F_{Tz} = F_{Bz} + F_L$, we obtain a relation for the buoyancy force as

$$\frac{F_{Bz}}{F_{gz}} = \frac{1}{1 - \alpha} \left(\frac{F_{Tz}}{F_{gz}} - \alpha \right). \quad (16)$$

Predictions of the correlation for the buoyancy force using Eq. (16) are shown as a dashed line in Fig. 10, and the difference between the dashed line and the dotted line shows the contribution of lift to the upward force, which is small. The predictions of the correlation are slightly higher than our computed values. A fit of Eq. (14) to the data is also shown in Fig. 10, and the coefficients obtained from fitting are $c_1 = 20.3$, $c_2 = 2.11$, $R_1 = 0.25$, and $R_2 = 4.17$.

Finally, consider the calculations based on Archimedean buoyancy for which the buoyancy force is given by $F_{Bz} = \rho \phi V_E g_z$, where V_E is the effective volume of the intruder, taking into account the excluded volume around it. The scaled buoyancy force is then

$$\frac{F_{Bz}}{F_{gz}} = \frac{\phi V_E}{V_i}. \quad (17)$$

The increase in the height of the flowing layer on adding a single intruder of size $S = 4$ is shown in Fig. 11. Similar results are obtained for other size ratios (S). The scaled Archimedean buoyancy using the effective volume computed using this method is shown in Fig. 10. We also calculate the Archimedean buoyancy using two different estimates of the effective volume: (1) assuming

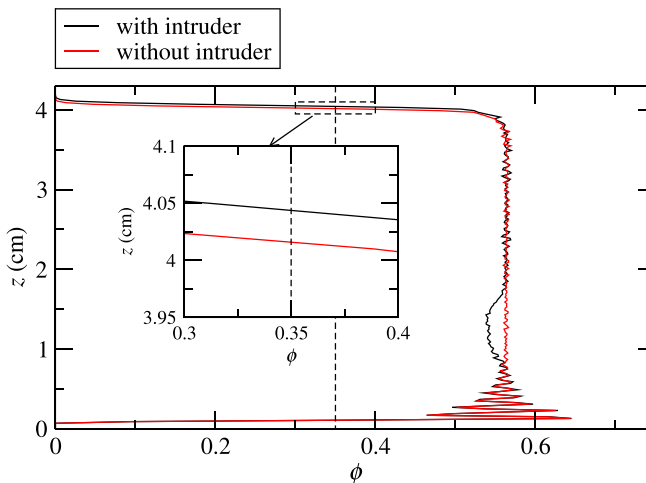


FIG. 11. Volume fraction profiles $[\phi(z)]$, with an intruder of size ratio $S = 4$ and without an intruder. Inset: A magnified view of the increase in the free surface height on adding an intruder.

the effective volume to be equal to the partial molar volume obtained by Kumar *et al.* [13], and (2) using the Voronoi tessellation-based data reported by van der Vaart *et al.* [11]. The results are also shown in Fig. 10 and are close to those based on the intruder addition method. All three results are smaller than the computed buoyancy force, indicating that Archimedean buoyancy is not large enough to predict the rise of the intruder, even when the effective volume is considered, as noted in previous works [11,15]. The lift force cannot account for the difference since it acts in a direction opposite to the buoyancy force, as shown in Eq. (15). The causes of the lift force and the buoyancy force are discussed next.

D. Microscale analysis

We consider the flow and stress in a local region around an intruder of size ratio $S = 4$ for both flows. In the results presented below for the shear flow, we take the wall velocity to be $U = 50$ cm/s and the pulling force to be $F_p = 40$ dyn. For the inclined plane flow, we take the inclination angle to be 25° and the pulling force to be $F_p = 1.74$ dyn, at which slip velocity is $u_s = 0$. The shear flow simulations provide insights into the causes of the lift force, while the inclined plane simulations give insights into the causes of the buoyancy force.

Figure 12 shows the variation of the relative velocity ($v_{xr} = v_x - u_i$) and the normal stress (σ_{zz}) with height relative to the intruder center, $z_r = z - z_i$, along a vertical line passing through the center of the intruder. The bins, of dimension $d \times d \times 0.2d$, used for computing the profiles are shown schematically in the inset in Fig. 12(a). The dashed lines show the profiles in the absence of the intruder. The velocity profiles [Figs. 12(a) and 12(b)] indicate that the influence of the intruder is limited to a short distance ($2d - 3d$) from the surface of the intruder, and most of the change is due to slip of the first layer of particles adjacent to the intruder. The profiles are not similar to the Stokes' flow profiles. The slip is symmetric for the inclined plane flow since the slip velocity is $u_s = 0$, but not for the shear flow for which the slip velocity is positive. The stress profile shows large fluctuations near the surface of the intruder with maximum values about six times the mean value for both flows [Figs. 12(b) and 12(d)].

Figure 13 shows the variation of solid fraction (ϕ) and the inward normal velocity relative to the intruder (v_n), computed for a vertical slice of thickness d centered on the intruder centroid, using bins of cross section $0.2d \times 0.2d$ in the $x_r z_r$ plane and thickness d , shown schematically in the inset of Fig. 13. The shear flow and the inclined plane flow results are qualitatively similar, though

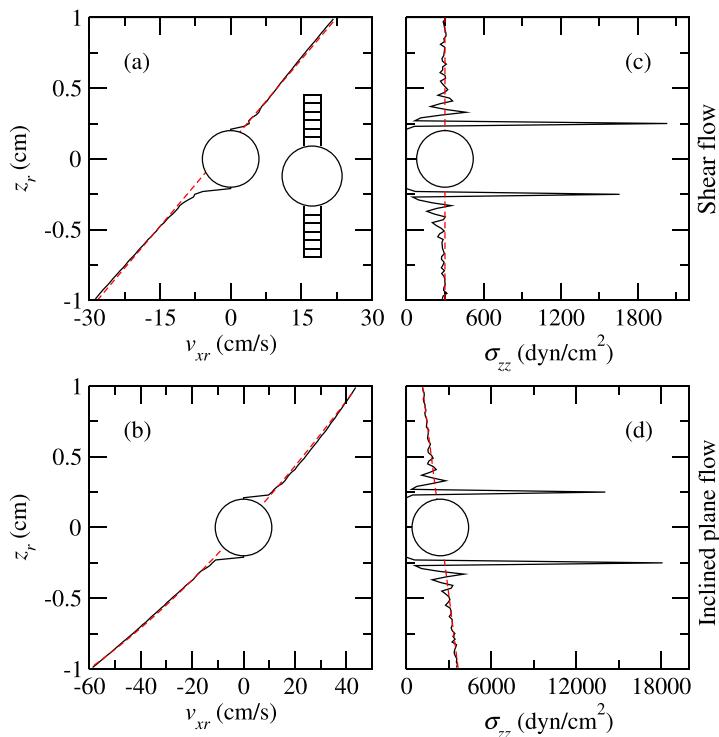


FIG. 12. Variation of the relative velocity (v_{xr}) and normal stress (σ_{zz}) with height from the center of the intruder (z_r) for size ratio $S = 4$. (a),(c) Shear flow for $U = 50$ cm/s and $F_P = 40$ dyn. (b),(d) Inclined plane flow for inclination angle $\theta = 25^\circ$ and $F_P = 1.74$ dyn ($u_s = 0$).

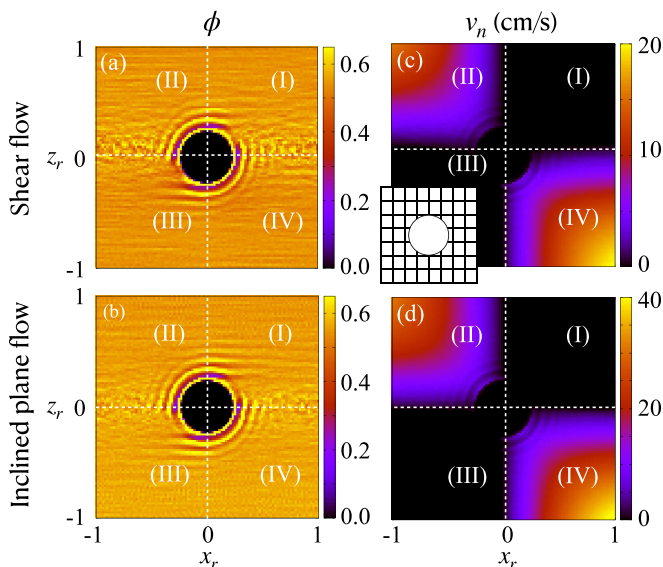


FIG. 13. The distribution of the solid fraction (ϕ), and inward normal velocity (v_n) in a vertical plane passing through the center of the intruder of size ratio $S = 4$ for (a),(c) shear flow for wall velocity $U = 50$ cm/s and (b),(d) inclined plane flow for inclination angle $\theta = 25^\circ$. Inset: Schematic of the bins used in the computations, with bin dimensions $0.2d \times d \times 0.2d$.

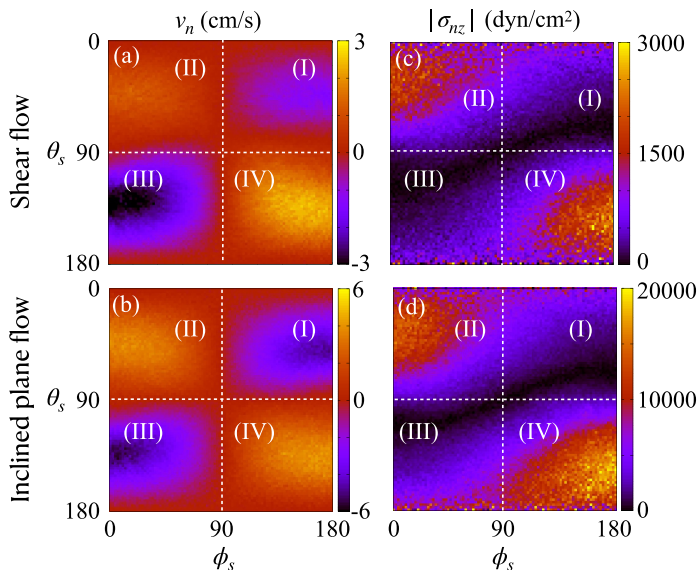


FIG. 14. Variation of (a),(b) the inward normal velocity (v_n) and (c),(d) the upward stress ($|\sigma_{nz}|$) at the surface of the intruder of size $S = 4$ with angles (θ_s, ϕ_s) in spherical coordinates for shear flow with wall velocity $U = 50$ cm/s (top row) and for inclined plane flow with inclination angle $\theta = 25^\circ$ (bottom row). The bin dimensions are $\Delta\theta_s = 2^\circ$, $\Delta\phi_s = 2^\circ$, and $\Delta r = 1.5d$.

the velocity magnitudes are significantly different. The solid fraction (ϕ) shows strong layering in the second and fourth quadrants near the intruder [Figs. 13(a) and 13(b)]. This is a consequence of the positive values of v_n in these quadrants [Figs. 13(c) and 13(d)]; the negative values of v_n are not shown for clarity.

Figure 14 shows the inward normal velocity (v_n) and the magnitude of the upward component of the total stress ($|\sigma_{nz}|$). The figure shows the variation of the variables over a hemispherical surface of the intruder in spherical coordinates (θ_s, ϕ_s) , where $\theta_s = 0$ corresponds to the north pole of the intruder and $\phi_s = 0$ to $x_r = -d_i/2$. In other words, the front hemispherical surface is mapped to a square area. The dimensions of the bins used are $\Delta\theta_r = \Delta\phi_r = 2^\circ$ and $\Delta r = 1.5d$. The inward normal velocity, for $v_n > 0$, is higher in quadrant IV relative to that in quadrant II for the shear flow due to the significant slip velocity [Fig. 14(a)]. For the inclined plane flow, the velocities in the two quadrants are nearly the same since the slip velocity $u_s = 0$ [Fig. 14(b)]. The magnitude of the upward component of the total stress on the surface is low over most of the surface, except for patches of high stress in quadrants II and IV, with the stress in quadrant IV being higher for both flows [Figs. 14(c) and 14(d)]. The higher stress in quadrant IV for the shear flow is due to the higher collisional stress due to the higher relative velocity in the quadrant because $u_s > 0$. In contrast, the higher stress for the inclined plane flow is due to the stress variation with height and the concentration of the stress in small patches on the surface of the intruder. The stress for the inclined plane flow is significantly larger than the shear flow case.

Figure 15 shows the variation of the inward normal relative velocity (v_n) and the upward component of the total stress on the surface of the intruder (σ_{nz}) with angle (β) for the shear flow, acting on the surface of the intruder in a vertical slice passing through the center of the intruder. The bins used in the computations have dimensions $\Delta\beta = 2^\circ$, $\Delta r = 1.5d$, and width d , and are shown schematically in the figure. The inward normal velocity has peaks in the second and fourth quadrants, and the dashed lines show the magnitudes of the peak values of v_n in quadrant II. The peak in quadrant IV is slightly higher than that in quadrant II due to the positive slip velocity.

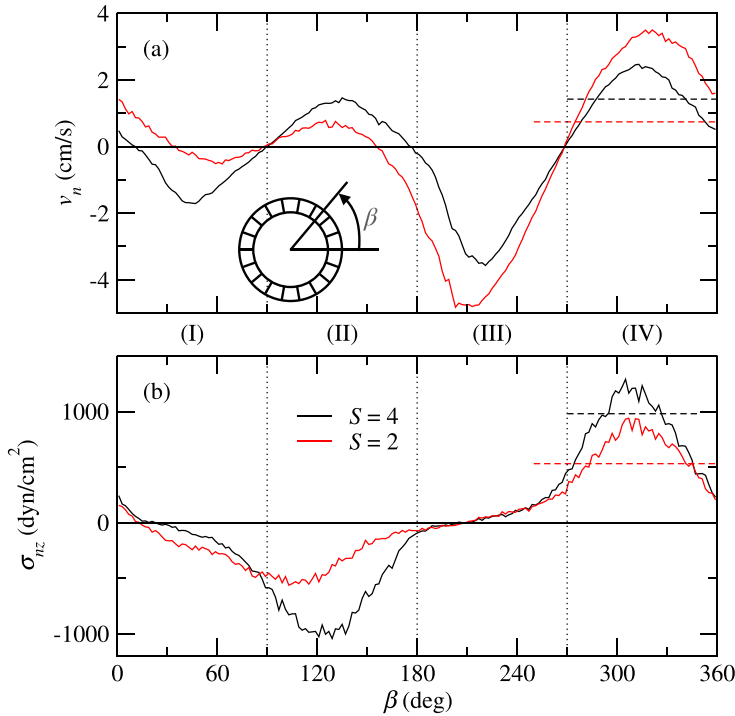


FIG. 15. Variation of (a) the inward normal velocity (v_n) and (b) the total upward stress (σ_{nz}) at the surface of the intruder with angle (β) defined in the schematic view shown in the inset with bins of dimensions $\Delta\beta = 2^\circ$ and $\Delta r = 1.5d$. The data are for intruder sizes $S = 4$ and $S = 2$, and wall velocity $U = 50$ cm/s for the shear flow. The dashed lines correspond to the magnitude of the minimum values of the stress.

The stress is nearly zero in the first and third quadrants, acts downward in the second quadrant, and acts upward in the fourth quadrant. The dashed lines in the figure show the magnitudes of the stress minima in the second quadrant and show that the upward stress is larger than the downward stress. The net upward force, resulting from a relatively higher inward normal velocity in quadrant IV, is then responsible for granular lift. Data for an intruder size $S = 2$, for which the lift force is higher than that for $S = 4$, are also shown in Fig. 15. The difference in values v_n of quadrant IV and quadrant II are higher for $S = 2$, resulting in a higher net upward stress. This reinforces the conclusion that the higher inward normal velocity in quadrant IV due to a positive slip velocity ($u_s > 0$) is the cause of granular lift.

Figure 16 shows similar graphs for the inclined plane for an intruder of size $S = 4$. The inward normal velocity (v_n) is nearly the same in quadrants II and IV [Fig. 16(a)], which is expected since the slip velocity is zero, $u_s = 0$. The variation of the total stress in the z direction (σ_{nz}) with angle β is shown in Fig. 16(b). The stress acts downward in quadrant II and upward in quadrant IV, and is nearly zero in the other two quadrants. The dashed line shows the magnitude of the minimum stress in quadrant II. The maximum net upward stress, given by the height of the peak above the dashed line, gives a measure of the buoyancy force. The z component of the hydrostatic force on the intruder for $S = 4$, considering its volume to be the effective volume (V_E), is also shown in the figure. The maximum net upward stress, in this case, is about two orders of magnitude smaller since the stress is assumed to be hydrostatic over the surface of the intruder. Thus, shearing causes strong layering of particles in quadrants II and IV, leading to stress concentration in these quadrants, and these high stresses generate buoyancy forces larger than the predictions of Archimedean buoyancy.

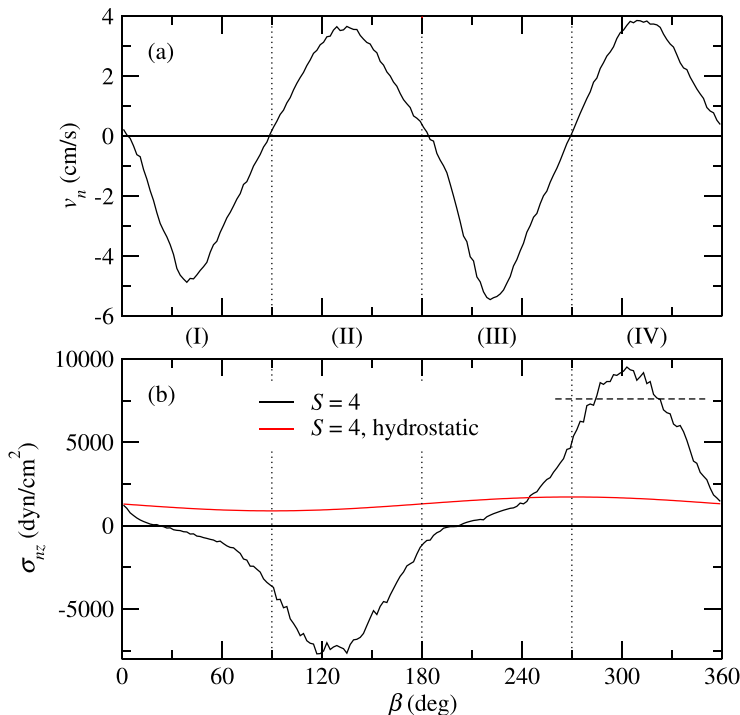


FIG. 16. Variation of (a) inward normal velocity (v_n) and (b) the total upward stress (σ_{nz}) at the surface of the intruder with angle β , as defined in Fig. 15. The data are for intruder size $S = 4$, and inclination angle $\theta = 25^\circ$ for the inclined plane flow. The dashed line corresponds to the magnitude of the minimum value of the stress. The predicted pressure on the intruder surface for a linear variation of the pressure with height (hydrostatic) is also shown.

The results of this section show that the velocity disturbance is confined to a small region around the intruder, and the stress is localized with large fluctuations of the stress relative to the mean value. The rapid decrease in the velocity disturbance with distance from the intruder indicates that the inertial contribution required for the Saffman lift is negligible. The lift force in the granular system is, instead, due to the higher collisional stress in the fourth quadrant due to the higher inward normal velocity generated by the positive slip velocity. The buoyancy force is larger than the Archimedean buoyancy force due to the high concentration of stress in the second and fourth quadrants, compared to the hydrostatic stress on the surface.

E. Application to segregation modeling

Finally, we show how the computational results for buoyancy, lift, and drag can be used to formulate continuum models for the segregation flux in binary mixtures of large and small particles in a shear flow under gravity, following the approach given in [9]. There is no pulling force on the particles ($F_p = 0$). The segregation flux can then be incorporated in the convective-diffusion balance equation to compute the concentration distribution of the large particles in the system.

Consider first the dilute limit in which the volume concentration of large particles, $v_i = \phi_i/\phi$, is low, with ϕ_i being the solid fraction of the large particles. In this case, the segregation flux of the large particles in the z direction is

$$J_{iz}^0 = v_{Si}v_i, \quad (18)$$

where v_{si} is the segregation velocity of the large particles given by

$$v_{si} = (F_{Bz} + F_L - F_{gz})/\xi. \quad (19)$$

On substituting for F_L and F_{Bz} using Eqs. (13) and (14), we get

$$v_{si} = [f(S) - 1]m_i g \cos \theta / \xi + (A - BS)u_s. \quad (20)$$

From the force balance in the z direction, the slip velocity is obtained as

$$u_s = [f(S) - 1]m_i g \sin \theta / \xi. \quad (21)$$

Combining Eqs. (20) and (21), we get the segregation flux for small volume concentrations of the large particles as

$$J_{iz}^0 = \frac{m_i g [f(S) - 1]}{C_D \eta d_i} [\cos \theta + (A - BS) \sin \theta] v_i. \quad (22)$$

Given the small values of the coefficients A , B and $\sin \theta$, the contribution of the lift force to the segregation flux is small, as seen in Fig. 10.

To extend the above expression for the segregation flux to higher volume concentrations of the large particles, we may use the empirical correction proposed by Kumar *et al.* [13],

$$J_{iz} = J_{iz}^0 (1 - v_i)(1 + k v_i), \quad (23)$$

where $k \approx S$ is an empirical coefficient. The correction was shown to give good predictions of the concentration profile, $v_i(z)$, for $S \leq 2$. A more rigorous approach would involve computation of the buoyancy, lift, and drag forces for mixtures with different concentrations of the large particles instead of a single intruder, as done by Duan *et al.* [19] for the segregation force.

IV. CONCLUSIONS

Forces on an intruder in two flows, i.e., a shear flow at constant pressure and an inclined plane flow driven by gravity, are computed using DEM simulations. The force normal to the flow direction is obtained using a linear spring, and a pulling force is applied in the flow direction to generate substantial slip velocities. The system size is taken to be sufficiently large, and averaging is taken over long enough times to ensure accurate results. Lift and drag forces are obtained from the shear flow computations, and lift, drag, and buoyancy forces are obtained from the inclined plane flow computations, with the buoyancy force defined as the upward force when there is no slip velocity ($u_s = 0$).

The computed drag force was found to follow Stokes' Law scaling over the range of velocities considered, and data for both systems, for varying intruder sizes and shear rates, collapse to a single line, despite significantly different apparent viscosities in the two systems. The computed granular lift force was found to act in a direction opposite to the Saffman Lift and to be 10–30% of the drag force in the magnitude. The ratio of the lift force to the drag force (R) was found to vary linearly with the intruder size ratio as $R = A - BS$, and all the data for different sizes and shear rates collapsed to a single line for different intruder sizes and shear rates for both systems. The buoyancy forces on the intruder, computed in directions normal to the flow and the direction of flow, when scaled with the corresponding component of the weight of the intruder, are found to depend only on the size ratio (S). Again, all the data for the inclined plane flow collapse to a single curve and are close to, but slightly lower than, the correlation of Jing *et al.* [14]. The buoyancy force is larger than the weight of intruders with a size ratio in the range $S \in (1, 4)$ and is responsible for the rise of the intruder. The lift force does not contribute to the rise since it is much smaller in magnitude and acts in a direction opposite to the buoyancy.

Analysis of the velocity profiles in the neighborhood of the intruder for both systems shows that they are not similar to Stokes flow, and there is significant wall slip at the intruder surface as well as high-stress fluctuations near the intruder—as much as six times the mean stress. The

stress distributions for the shear flow indicate that there are high-stress patches in the second and fourth quadrants of the intruder caused by particle layering due to the inward normal velocity of the base particles in these regions. The lift force is caused by the upward stress in the fourth quadrant being higher than the downward stress in the second quadrant, which results from the higher inward normal velocity in the fourth quadrant caused by a positive slip velocity ($u_s > 0$). The stress distributions for the inclined plane flow with a pulling force at which there is no slip velocity ($u_s = 0$) again show patches of high stress in the second and fourth quadrants because of the inward normal velocities in these regions. The upward stress in the fourth quadrant is larger than the downward stress due to the hydrostatic gradient causing the upward buoyancy force. The magnitude of this buoyancy force is significantly larger than the buoyancy force (even after accounting for the effective volume) due to the large stress concentration in patches on the surface of the intruder.

The results presented here for a single intruder are applied to model segregation in mixtures with a low volume concentration of large particles. The results indicate that size segregation in such dilute systems of particles of different sizes and equal density is primarily due to buoyancy. However, lift forces could play a role if the inclination angle is sufficiently large so as to cause a significant slip velocity. The model for segregation is extended to the entire range of concentrations of the large particles by means of an empirical correction factor applied to the single particles' values. However, for a more accurate estimate of the buoyancy, drag, and lift forces, a similar computational approach as used here, but with mixtures of large particles of different concentrations, would be required, as done by Duan *et al.* [19] for the segregation force.

-
- [1] J. M. Ottino and D. V. Khakhar, Mixing and segregation of granular materials, [Annu. Rev. Fluid Mech. **32**, 55 \(2000\)](#).
 - [2] M. Woodhouse, A. R. Thornton, C. G. Johnson, B. Kokelaar, and J. Gray, Segregation-induced fingering instabilities in granular free-surface flows, [J. Fluid Mech. **709**, 543 \(2012\)](#).
 - [3] C. G. Johnson, B. P. Kokelaar, R. M. Iverson, M. Logan, R. G. LaHusen, and J. M. N. T. Gray, Grain-size segregation and levee formation in geophysical mass flows, [J. Geophys. Res. Earth Surf. **117**, F01032 \(2012\)](#).
 - [4] J. M. N. T. Gray, Particle segregation in dense granular flows, [Annu. Rev. Fluid Mech. **50**, 407 \(2018\)](#).
 - [5] J. A. Drahn and J. Bridgwater, The mechanisms of free surface segregation, [Powder Technol. **36**, 39 \(1983\)](#).
 - [6] S. B. Savage and C. K. K. Lun, Particle size segregation in inclined chute flow of dry cohesionless granular solids, [J. Fluid Mech. **189**, 311 \(1988\)](#).
 - [7] J. T. Jenkins and F. Mancini, Kinetic theory for binary mixtures of smooth, nearly elastic spheres, [Phys. Fluids **1**, 2050 \(1989\)](#).
 - [8] A. Tripathi and D. V. Khakhar, Numerical Simulation of the Sedimentation of a Sphere in a Sheared Granular Fluid: A Granular Stokes Experiment, [Phys. Rev. Lett. **107**, 108001 \(2011\)](#).
 - [9] A. Tripathi and D. V. Khakhar, Density difference-driven segregation in a dense granular flow, [J. Fluid Mech. **717**, 643 \(2013\)](#).
 - [10] F. Guillard, Y. Forterre, and O. Pouliquen, Scaling laws for segregation forces in dense sheared granular flows, [J. Fluid Mech. **807**, R1 \(2016\)](#).
 - [11] K. van der Vaart, M. P. van Schrojenstein Lantman, T. Weinhart, S. Luding, C. Ancey, and A. R. Thornton, Segregation of large particles in dense granular flows suggests a granular Saffman effect, [Phys. Rev. Fluids **3**, 074303 \(2018\)](#).
 - [12] L. Staron, Rising dynamics and lift effect in dense segregating granular flows, [Phys. Fluids **30**, 123303 \(2018\)](#).

- [13] A. Kumar, D. V. Khakhar, and A. Tripathi, Theoretical calculation of the buoyancy force on a particle in flowing granular mixtures, *Phys. Rev. E* **100**, 042909 (2019).
- [14] L. Jing, J. M. Ottino, R. M. Lueptow, and P. B. Umbanhowar, Rising and sinking intruders in dense granular flows, *Phys. Rev. Res.* **2**, 022069(R) (2020).
- [15] M. van Schrojenstein Lantman, K. Van Der Vaart, S. Luding, and A. R. Thornton, Granular buoyancy in the context of segregation of single large grains in dense granular shear flows, *Phys. Rev. Fluids* **6**, 064307 (2021).
- [16] L. Jing, J. M. Ottino, R. M. Lueptow, and P. B. Umbanhowar, A unified description of gravity-and kinematics-induced segregation forces in dense granular flows, *J. Fluid Mech.* **925**, A29 (2021).
- [17] D. V. Khakhar, J. J. McCarthy, and J. M. Ottino, Mixing and segregation of granular materials in chute flows, *Chaos: Interdisc. J. Nonlin. Sci.* **9**, 594 (1999).
- [18] P. G. Saffman, The lift on a small sphere in a slow shear flow, *J. Fluid Mech.* **22**, 385 (1965).
- [19] Y. Duan, L. Jing, P. B. Umbanhowar, J. M. Ottino, and R. M. Lueptow, Segregation forces in dense granular flows: Closing the gap between single intruders and mixtures, *J. Fluid Mech.* **935**, R1 (2022).
- [20] A. P. Thompson, H. M. Aktulga, R. Berger, D. S. Bolintineanu, W. M. Brown, P. S. Crozier, P. J. in 't Veld, A. Kohlmeyer, S. G. Moore, T. D. Nguyen, R. Shan, M. J. Stevens, J. Tranchida, C. Trott, and S. J. Plimpton, LAMMPS - a flexible simulation tool for particle-based materials modeling at the atomic, meso, and continuum scales, *Comput. Phys. Commun.* **271**, 108171 (2022).
- [21] L. E. Silbert, D. Ertaş, G. S. Grest, T. C. Halsey, D. Levine, and S. J. Plimpton, Granular flow down an inclined plane: Bagnold scaling and rheology, *Phys. Rev. E* **64**, 051302 (2001).
- [22] H. A. Stone, Philip Saffman and viscous flow theory, *J. Fluid Mech.* **409**, 165 (2000).